JACS
JOURNAL OF THE AMERICAN CHEMICAL SOCIETY
pubs.acs.org/JACS Article

S = 1/2 Chain in $BiVO_3F$: Spin Dimers versus Photoanodic Properties

Olivier Mentré,* Miguel A. Juárez-Rosete, Sebastien Saitzek, Cintli Aguilar-Maldonado, Marie Colmont, and Ángel M. Arévalo-López

Cite This: *J. Am. Chem. Soc.* 2021, 143, 6942−6951 Read Online

ACCESS | Metrics & More | Article Recommendations | SI Supporting Information

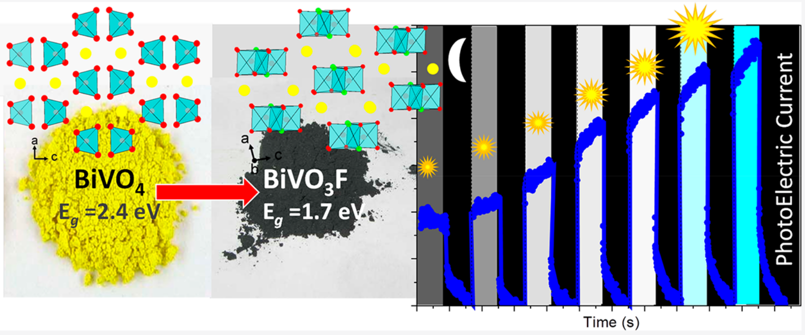

ABSTRACT: $BiVO_3F$ was prepared, characterized, and identified as a unique example of bismuth vanadyl oxyhalide with paramagnetic V^{4+} centers. Its crystal structure shows 1D magnetic units with rare alternation of edge-sharing O−O and F−F μ_2 bridges along the octahedral chains. Structural pairing across the O_2 edges induces antiferromagnetic spin dimers ($S = 0$) with $J/K_b \approx 300$ K, ∼15 times greater than the exchange across the F_2 bridges, within a non-ordered magnetic ground state. Despite multiple compositional, structural, and electronic analogies with the $BiVO_4$ scheelite compound, one of the most promising photoanodes for solar water splitting, the photoactivity of $BiVO_3F$ is relatively modest, partially due to this electronic pairing benefitting fast electron−hole recombination. Similar to monoclinic VO_2, the V^{4+} spin dimerization deters the singlet → triplet electronic photoexcitation, but results in potential carrier lifetime benefits. The reduction of the bandgap from an E_g of ∼2.4 eV to ∼1.7 eV after incorporation of d^1 cations in $BiVO_4$ makes $BiVO_3F$ an inspiring compound for local modifications toward an enhanced photoactive material. The direct d → d transition provides a significant enhancement of the visible light capture range and opens a prospective route for the chemical design of performant photoanodes with a mixed anionic sublattice.

■ INTRODUCTION

Inorganic metal oxide fluorides have significant importance in recent technologies, such as energy storage,[1] microelectronics,[2−4] photonics, and catalysis.[5] Within this frame, the recent discovery of the $n = 1$ Aurivillius oxyfluoride $[Bi_2O_2][CoF_4]$ phase has opened even wider perspectives about novel multiferroics[6] by combining ferroelectric opportunities brought by the standard Bi^{3+} lone-pair effect and magnetic ordering resulting from the presence of magnetic ions in the $[CoF_4]$ perovskite block, mimicking $BiFeO_3$. Besides, due to the similarity of their ionic radii, the replacement of O^{2-} by F^- in flexible structural motifs such as perovskite or rocksalt blocks allows an O^{2-}/F^- random distribution and may accommodate anionic vacancies (v) and subtle metal displacements, as in $AM(O,F,\mathbf{v})_3$, $BaInO_2F$, or $FeO_{1-x}F_x$.[7] However, the 1D (chain-based) oxyfluoride topology[8] often induces anionic ordering, especially when surrounded by lone-pair ions with anisotropic electronic density clouds. Such oxyfluoride chains have provided excellent models for low-dimensional magnetism, due to the minimization of electronic delocalization through electronegative F^- bridges.[9] To date, the concerned Bi−V−O−F chemical system is almost empty, since only 3D F^--doped $BiVO_4$[10] and Bi_2VO_5F[11] have been reported so far. In the former, the F^- doping enables enhanced photoelectrochemical performances, while the latter corresponds to F^- doping in the perovskite slabs of the well-known 2D $Bi_4V_2O_{11}$, the best high-temperature ionic conductor ever, and, thus, induces a minor amount of V^{4+}.

We report here the synthesis of the first bismuth vanadyl oxyhalide $BiVO_3F$. It shows a unique alternation of O_2 and F_2 bridges in V^{4+} ($S = 1/2$) chains, which offers nice perspectives for the design of materials straddling the border between finite clusters and periodic magnetic lattices. In addition, the compositional analogy between $BiVO_3F$ and $BiVO_4$, one of the most promising photoanodes for water splitting,[12] suggests

Received: January 22, 2021
Published: April 28, 2021

ACS Publications

https://doi.org/10.1021/jacs.1c00621

photoelectronic activities. In the latter oxide, the conduction band (CB) containing $3d^0$ V^{5+} hybridized with O 2p states form large polarons, beneficial as catalytic redox centers for screening the carrier−carrier and carrier−defect scattering in favor of long carrier lifetime[13] together with raising the valence band (VB) edge and bandgap reduction from the low binding energy states of Bi^{3+} $6s^2$ electrons. Strategies for enhanced $BiVO_4$ photocatalytic properties have been proposed by tuning its electronic structure with chemical substitution using either less electronegative anions (S^{2-}, N^{3-}) or cations with occupied low binding energy d^{10} states (Cu^+, Ag^+) with inherent chemical problems.[13] Theoretical incorporation of unfilled d^n cations (d^1 Cr^{5+}, Mo^{5+}, W^{5+}) has shown favorable separation of photoexcited electron−hole pairs, giving opportunities for the electrons to transit from VB to CB for the reduction of the electron effective mass and lengthening of the carrier diffusion.[14] Similar to the Fe^{3+}-doped TiO_2 situation, the dopant d−d transitions offer a visible light response due to narrowing of the band gap, trapping of electrons and holes, and decreasing exciton recombination.[15] Closer to the title compound, V^{4+} self-doped $BiVO_{4-\delta}$ nanorods prepared in solvothermal conditions also show enhanced organic pollutant degradation under visible light assigned to the improved electron−hole separation.[16] Similar photocalatytic performances have been reported for microporous F-doped $BiVO_4$ obtained after autoclave reaction with NH_4F;[17] however, no reliable crystallographic evidence of the intrinsic vanadium reduction has been given, along with a weak bandgap evolution, thus suggesting synergistic surficial and microstructural effects.

The introduction of d^1 V^{4+} species with direct d−d excitations and narrowed bandgap in $BiVO_3F$ makes this phase a model to investigate its characteristic electronic structure features. It also opens a new route and inspiring concepts to tune photoanodic properties by mixed anion content control.[18]

RESULTS AND DISCUSSION

1D Crystal Structure. Single crystals of $BiVO_3F$ have been grown through the hydrothermal route from a 2:1 mixture of VF_3 (or VF_4) and Bi_2O_3 in a dilute HF solution. $BiVO_3F$ can be obtained as the main phase when working from a stoichiometry of Bi:V = 1:2, while working in stoichiometric conditions results in the major copresence of BiOF and $Bi_7F_{11}O_5$ bismuth oxyfluorides. Using the former procedure either single crystals can be selected or a ∼90 wt % polycrystalline product can be achieved after several sonication in ethanol/separation stages from the latter (see details in the Supporting Information, S1). Contrarily to the reported F^--doped $BiVO_4$ samples,[17] announced with a scheelite lattice independent of the Bi/F ratio, our results evidence drastic changes driven by V^{4+} and F^- incorporation in the lattice. In this prior work,[17] it is plausible that the final firing stage in air at 450 °C favors surficial and microstructural V^{4+} and F^- defects only. The $BiVO_3F$ crystal structure was solved from single-crystal X-ray diffraction (XRD) data (R_{obs} = 1.81%, wR_{obs} = 2.05%) in the monoclinic $P2_1/n$ space group (a = 5.2621(6) Å, b = 4.9721(3) Å, c = 12.6149(7) Å, β = 95.590(2)°, V = 328.48(3) Å^3, Z = 4); see Supplementary Table S1 for details. The pertinent bond distances are given in Table 1 (CSD 2055766). The crystal structure consists of edge-sharing $_\infty[V^{4+}O_3F]^{3-}$ zigzag chains separated by Bi^{3+} cations; see Figure 1a and b. The asymmetric Bi^{3+} coordination is typical of $6s^2$ lone-pair (E) ions with a 3O + E basal plane and 2O + 2F axial ligands. The anions are clearly distinguished by their bond valence sums (BVS) with values between −1.82 and −2.26 for O1−3 and −0.97 for F; see Tables S2, S3, and S4.

Table 1. Interatomic Distances (Å) and Cation BVS for the $BiVO_3F$ Structure

bond	distance (Å)	bond	distance (Å)
Bi−O1	2.102(7)	V−O1	1.938(8)
Bi−O2	2.165(8)	V−O1	1.919(8)
Bi−O2	2.135(8)	V−O2	1.996(8)
Bi−O3	2.833(8)	V−O3	1.641(9)
Bi−O3	2.642(9)	V−F	1.991(7)
Bi−F	2.831(7)	V−F	2.154(7)
Bi−F	2.776(6)	$\sum_i S_i$	4.09(5)
$\sum_i S_i$	4.09(5)	$V-V_{(O2)}$	2.935(3)
		$V-V_{(F2)}$	3.320(3)

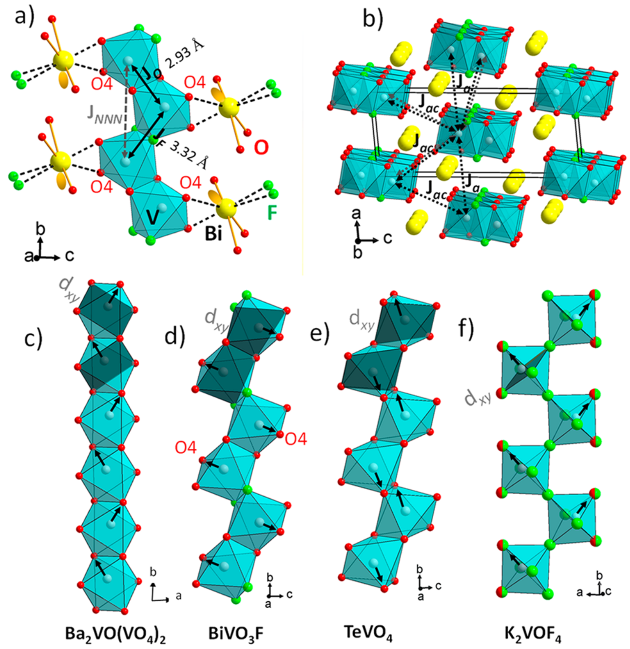

$Ba_2VO(VO_4)_2$ $BiVO_3F$ $TeVO_4$ K_2VOF_4

Figure 1. (a) $_\infty[V^{4+}O_3F]^{3-}$ zigzag chains of edge-sharing VO_4F_2 octahedra and interstitial Bi^{3+} with intrachain V−V couplings. (b) Main interchain exchanges considered. Comparison of vanadyl-chain topology and d_{xy} magnetic orbitals (darkened planes) in (c) $Ba_2VO(VO_4)_2$, (d) $BiVO_3F$, (e) $TeVO_4$, and (f) K_2VOF_4. The arrows point to the V═O short bonds.

The zigzag chains of $BiVO_3F$ are similar to those found in pyroxene, but rely on the *cis*−*trans* alternation of O−O and F−F μ_2 bridges along the *b*-axis. To the best of our knowledge, such sequential O−O and F−F bridges, along edge-sharing chains, have only been reported for $Na_2Fe(PO_4)F$,[19] $Fe(SeO_3)F$,[20] and $M_2(XO_3)F_2$ (M = Mn, Co, Ni, Cu; X = Te, Se),[21,22] where the oxygen ions are systematically corners of covalent oxo-anion groups in contrast with $BiVO_3F$. Despite its 1D crystal structure, a certain analogy with the 0D $BiVO_4$ exists due to the conservation of trigonal planar coordination for O1, O2, and O3 and the strongly acentric coordination of Bi^{3+} ions. The hypothetical topochemical $BiVO_4$ → $BiVO_3F$ transformation can be sketched in three main steps; see Figure 2. (i) Starting from the scheelite $BiVO_4$, the VO_4 groups are tilted and displaced toward each other by pairs. (ii) This leaves

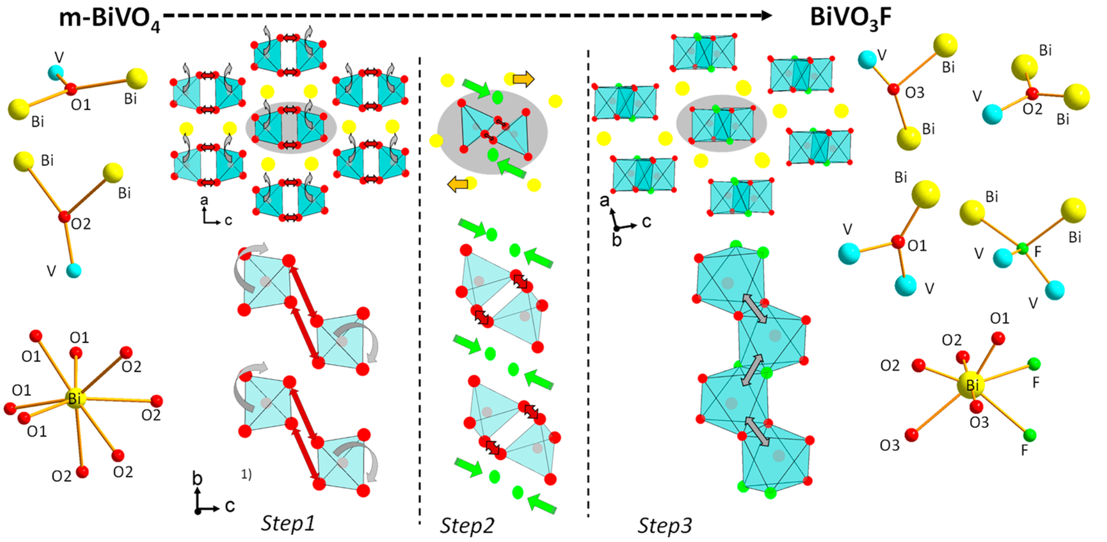

Figure 2. Details of the anion and Bi coordination and sketch of a hypothetical structural transformation of monoclinic $BiVO_4$ into $BiVO_3F$ in three steps according to the main text.

large voids for F^- insertion, i.e., $1F^-$ per VO_4, while the VO_4 approach tends to a common O−O edge. At this stage Bi^{3+} species would be displaced by a *push and pull* mechanism in the (*bc*) plane. (iii) The $BiVO_3F$ crystal structure will then merge O−O and F−F edges into 1D chains. This synopsis inspires the possibility of an experimental scenario by controlled fluorination.

$BiVO_3F$ offers a unique opportunity to examine the magnetic M−O−M versus M−F−M superexchange in a single material, without the engagement of oxygen ions encountering polyanions on the oxygen mediating corner, such as PO_4, SeO_3, and TeO_3 in the compounds mentioned above.[19−22] Here the octahedral distortion due to the V═O vanadyl bond externally to the chain axis and the O/F ordering shifts the superexchange angle from ∼90° as observed in some pyroxenes with similar canted chains[23] to V−O−V/V−F−V = 99.0(3)°/106.4(3)°, close to what is found in α-$TeVO_4$.[24,25] Despite the vanadyl bonds, a significant V^{4+}−V^{4+} pairing occurs along the chains, with distances of 2.93 and 3.32 Å across O−O and F−F bridges, respectively, despite short vanadyl bonds occurring externally to the V−V axis. The Coulombic repulsion associated with the $(V{=}O)^{2+}$ ions induces a crystal field splitting of the t_{2g} levels, such that the magnetic d^1 electrons lie mainly on the d_{xy} orbital according to the darkened planes in Figure 1c−f. Here, the zigzag edge-sharing chain topology and vanadyl arrangement of $BiVO_3F$ (Figure 1d) are compared to (i) linear chains in $Ba_2(VO)(VO_4)_2$[25] with weakened intrachain exchanges (V−O−V = 96°) but reinforced interchain couplings, Figure 1c; (ii) α-$TeVO_4$, a rare example of double-vanadyl bonds, toward a common edge with frustration between ferromagnetic (FM) nearest neighbor (NN) and antiferromagnetic (AFM) next nearest neighbor (NNN) exchanges along the chain axis, Figure 1e; (iii) the anion disordered K_2VOF_4, in which successive magnetic orbitals are perpendicular, along the chain, returning a paramagnetic behavior down to 2 K,[26] Figure 1f.

V^{4+} Spin Dimers. In $BiVO_3F$, the overlap between magnetic orbitals across the electronegative F−F bridge appears poorly efficient, with detrimental M−F long bond scaling effects;[27] see Figure 1d. In contrast, the d_{xy} orbitals are coplanar across the O−O μ_2 bridge, leaving an ideal topology for σ bonds. However, the V−V direct exchanges are expected to be weak because V−V is slightly above the reported V^{4+} critical distance of 2.9 Å.[28] The influence of the anion crystal field strength was first determined by extended Hückel tight-binding calculations (EHTB), changing the O^{2-} and F^- concentrations. Thus, we have conserved the experimental geometry of isolated $V_2O_6F_4$ units and compared it with the extremes, V_2F_{10} and V_2O_{10} units, and a drastic effect is observed on the crystal field splitting D_q and Racah B and C parameters. The standard quadratic split of $(V{=}O)^{2+}$ ions is exaggerated due to mixed O^{2-}/F^- coordination and to the structural pairing across the O_2 edge, but its fingerprint prevails in spectroscopic terms: ${}^2T_2 \rightarrow {}^2B_2$ and ${}^2E$; ${}^2E_g \rightarrow {}^2B_1$ and ${}^2A_1$ highlighted in Figure 3a for the experimental dimer.[29] The effect of the ligand field well reproduces the T_2/E_g increasing split from the *weak* fluoride crystal field D_q/B to the *medium* oxygen crystal field, similar to that reported for CrF_6/CrO_6 octahedral units.[30] In addition, the well-known tendency of electronegative F^- anions to lower the VB states was also evidenced, schematized by yellow arrows in Figure 3a. Focusing on the $V_2O_6F_4$ real unit shown in Figure 3b, the molecular orbital levels calculated by EHTB are shown in Figure 3c and d. For a dimer cluster, the commonly calculated energy splittings observed for most of the levels are due to the intermolecular orbital interaction based on the Hückel approximation. For increasing chain lengths, the bandwidth would approach the value of an infinite chain.[31] The highest occupied molecular orbitals (HOMOs) correspond to a magnetic $S = 0$ paired singlet, through degenerate σ^* V_{dxy}−(O_{py})−V_{dxy} and σ V_{dxy}−(O_{px})−V_{dxy} overlaps.

Magnetic Topology. The main identified magnetic exchanges for $BiVO_3F$ are shown in Figure 1, named J_O, J_F and J_{NNN} intrachain and J_{ac} and J_a interchain exchanges with respect to V−V distances less than 6 Å. Keeping in mind the particularly ambiguous choice of the Hubbard term U for V^{4+}, made on empirical grounds,[32] we mapped the total energies for a number of collinear spin configurations into a classical Heisenberg model to yield individual exchange couplings for different U = 2−4 eV and the effective on-site exchange interaction J_{eff} = 1 eV. Results are listed Table 2 together with the calculated bandgap and can be crosschecked to the

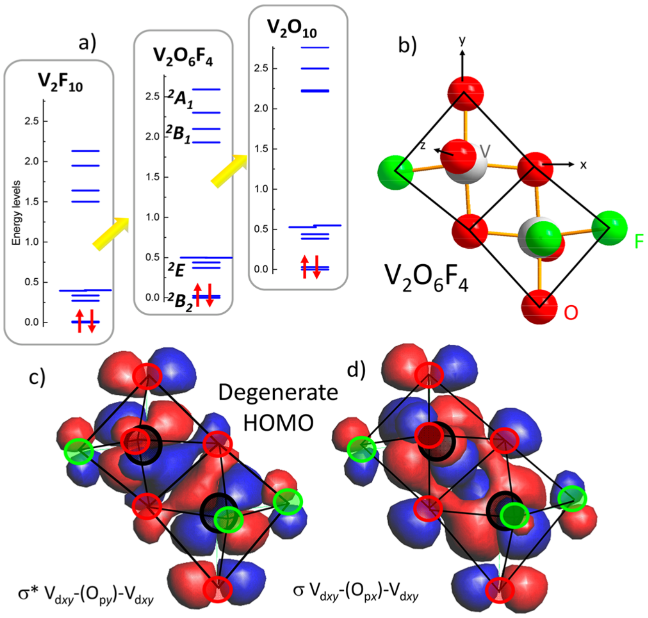

Figure 3. (a) EHTB molecular orbital energy levels calculated for isolated V_2F_{10}, $V_2O_6F_4$, and V_2O_{10} units; (b) structural view of the $V_2O_6F_4$ selected dimer; (c) σ^* $V_{dxy}-(O_{py})-V_{dxy}$ and (d) σ $V_{dxy}-(O_{px})-V_{dxy}$ degenerate HOMOs corresponding to the $^2B_2$ levels of (c).

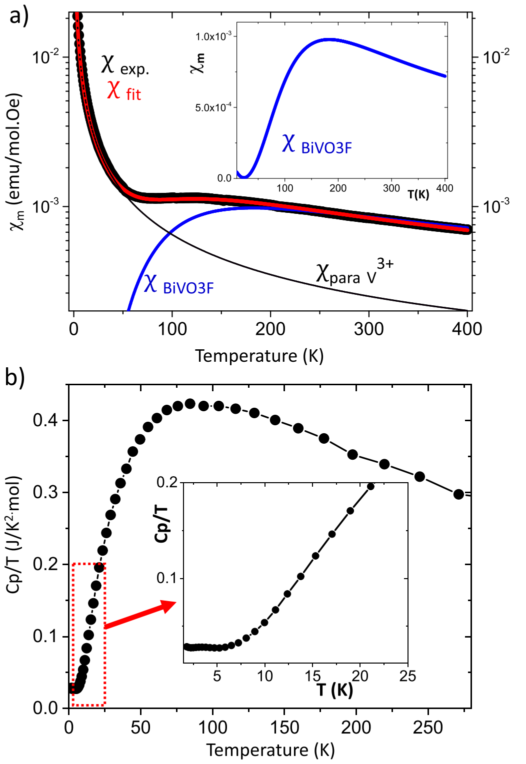

Figure 4. (a) Experimental and fitted $\chi(T)$ plot of $BiVO_3F$. (b) $C_p/T(T)$ curve with a zoom-in in the low-temperature domain in the inset proving no magnetic phase transition.

experimental values from our $\chi(T)$ fit and UV−visible reflectance spectroscopy. The superexchange (SE) J_O across the O−O bridge is predominant and larger than J_F by more than 1 order of magnitude for all U values, while the exchange J_{NNN} is very weak and almost U-independent. This results in a strong dimeric system already at room temperature, in accordance with the blank EPR signal measured from room temperature down to 4 K (X-band, Brüker ELEXYS E580), where the $S = 1$ state is poorly populated. The thermal dependence of the magnetic susceptibility was fitted by the analytical expression of χ_{chain} for an alternating J_O−J_F $S = 1/2$ reported by Hatfield[33] using the coefficient set for dominating dimers ($J_F \leq 0.4J_O$). The experimental and fitted plots are shown in Figure 4a. The interchain spin-exchange interactions were allowed in the molecular field expansion for the susceptibility χ_{chain}^{MF} at the paramagnetic regime (eq 1), with $\theta_{inter} = zS(S + 1)/3J_{inter}/k_b$, with the number of surrounding spins $z = 8$, as marked in Figure 1b.

$$\chi_{chain}^{MF} = \frac{\chi_{chain}(T)}{1 - \theta_{inter}\left[\frac{\chi_{chain}(T)}{C}\right]} \qquad (1)$$

Finally, the low-temperature paramagnetic tail was fitted using a Curie contribution assigned to V^{3+} ($S = 1$) impurities with respect to its "non-Kramers" silent EPR consistent with our blank spectra. Our best fit assuming $g = 2$ and $J_F/J_O = 5\%$, deduced from our ab initio DFT calculations, yields $J_O/k_b = 306(3)$ K, $J_F/k_b = 15.3$ K, and $J_{inter}/k_b = 21.7$ K with 6.0(5)% V^{3+} impurity. These correspond well to values calculated by DFT+U for U values between 2 and 3 eV. The heat capacity measurements also confirm the lack of magnetic ordering between 300 and 2 K, returning a true 1D magnetic system. However, the strong J_O suggests that most of the magnetic entropy remains engaged until high temperature and only a weak anomaly is expected but not detected; see $C_p/T(T)$ in Figure 4b. Indeed, besides the predominant AFM dimers across the O_2 bridges, the frustration occurring from J_F and J_{NNN} AFM interactions provides explicit arguments for low-temperature intrachain spin frustration. In addition, interchain FM J_{ac} and AFM J_a create additional frustrated J_a−J_{ac}−J_{ac} triangles and thus hamper any 3D magnetic ordering, and the dimerized topology predominates.

Electronic Band Structure. Besides EHTB calculations, the electronic structure analysis calculated by LDA+U offers a complementary vision in the extended 3D solid, out of discrete molecular orbital levels in the dimer cluster.

Table 2. Experimental and Calculated J and E_g values by LDA+U for U Ranging between 2 and 4 eV

J/k_b (K) and E_g (eV)	d(V−V), Å	U = 2 eV	U = 3 eV	U = 3.5 eV	U = 4 eV	exptl
J_O (1×)	2.93	387.1	231.2	177.9	135.5	306(3)
J_F (1×)	3.32	21.3	14.8	12.7	10.9	15.3
J_{NNN} (2×)	4.97	3.9	4.4	4.5	4.5	
J_a (4×)	5.75−5.84	37.6	21.1	15.4	10.8	21.7(3)
J_{ac} (4×)	5.26−5.58	−7.68	−5.6	−10.0	−4.5	
E_g		1.01	1.55	1.78	2.02	1.5−1.7

https://doi.org/10.1021/jacs.1c00621
J. Am. Chem. Soc. 2021, 143, 6942−6951

The density of states (DOS) and partial density of states (pDOS) are shown in Figure 5a for U = 3 eV in the ferromagnetic state, which enables screening the individual d orbital manifold within a unique type of vanadium in the unit cell. At this U value, it reproduces well the 1.5−1.7 eV UV−vis experimental bandgap shown in Figure 5b. The main VB between ∼−7 and −2 eV displays the same characteristics as what was reported for monoclinic $BiVO_4$.[34] It is primarily of O 2p character, where all O1, O2, and O3 atoms have a distorted triangular plane geometry (see Figure 2), similar to the oxygen coordinations in $BiVO_4$ of primary importance for its band texture with hybridized sp^2 and unhybridized 2pπ oxygen orbitals. At the top of the VB block, the contribution is mostly from O 2pπ nonbonding states. A sharp contribution of mixed Bi 6s and Bi 6p orbitals at −1.8 eV emphasizes the standard lone-pair stereoactivity. The bottom and middle of this VB block contain V 3d states hybridized with F^- and O^{2-} orbitals, respectively, as expected for more ionic V−F bonds. Around 1.1 eV above the main VB contribution and just below the Fermi level the V^{4+} d^1 spin-*up* $^2B_2$ state is trapped in a sharp pocket, similar to monoclinic VO_2 with a spin-Peierls dimerization reminiscent of $BiVO_3F$.[35] The CB is also split, with the very sharp lower part (around 1.5 eV) formed by antibonding vanadium ^2E levels mixed with oxygen states and minor contributions of F and Bi p states for both the minority and majority spins. At higher energies (>2.5 eV), the $^2B_1$ and $^2A_1$ vanadium states are mixed with Bi and O contributions, according to antibonding V−O and Bi−O σ^* overlap. This results in a band topology mixing both scheelite- $BiVO_4$ and monoclinic-VO_2 characteristics and allows for two allowed sets of d → d transitions, experimentally observed and labeled as (1) and (2) in Figure 5. The concerned localized states are at the top of the VB and bottom of the CB, similar to defect levels in doped semiconductors, and may serve as carrier traps during photoexcitation. This offers solutions for 3d orbitals too high in the conduction band for d^0-based semiconductors. $BiVO_3F$ bandgap narrowing and d−d transitions favor water splitting, allowing the transition and increasing the capture of visible light, following the strategy of d^n cation doping in $BiVO_4$ or TiO_2.[14−17]

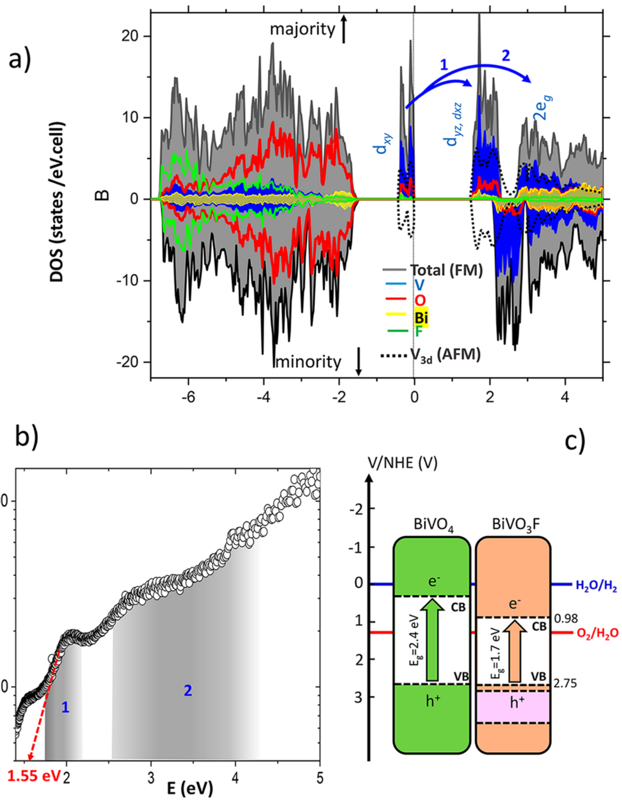

Figure 5. (a) Total and atomic resolved projected DOS for $BiVO_3F$ (U = 3 eV, FM/AFM spin-polarized configuration). (b) Diffuse-reflectance spectra with a Tauc plot calculation giving E_g = 1.55 eV. The gray areas denote the analogy with the DOS structure. (c) Band edge estimation (versus NHE) for $BiVO_4$ and $BiVO_3F$.

Only few works have been focused on the magnetic influence on photoactive properties and concern mainly (i) the magnetic photocatalysts to facilitate the catalyst separation from the reactant liquid phase[36] or (ii) more recently the suppressing of photoinduced charge recombination via Lorentz force using an external magnetic field.[37]

Here, the strong spin polorization arising from the spin AFM exchange within dimers may also offer extra advantages. Indeed, it was recently shown for deficient $Ti_{1-\delta}O_2$ that spin-polarized electrons can reduce the recombination of photo-induced electron−hole pairs by spin reversal in the CB due to spin−orbit coupling and hyperfine interactions, as observed in deficient TiO_2[38] and similar to a phosphorescence ingredient. In $BiVO_3F$, an equivalent scenario is available for the excitation restricted in individual dimers, from the singlet S = 0 to triplet S = 1. After photoexcitation and spin reversal, the electron−hole recombination is thus inhibited by the lack of spin-down in a spin-polarized environment. Figure 5a shows the DOS for vanadium d-levels calculated for an AFM *up*−*down* spin-polarized sequence along the edge-sharing chain very close to the DOS for AFM monoclinic VO_2.[39] The probability to excite two d^1 electrons in the same dimer is weak. After reversal of a single excited electron (↓), it must propagate and annihilate with the next excited dimer with down spin-holes (↓), which guaranty carrier diffusion. Of course, this is again a "double-edge sword", in the sense that the primary electronic excitation itself is hampered by the strong AFM magnetic exchanges holding robust S = 0 dimeric singlets as the stable state.

As detailed by Butler and Ginley,[40] empirical calculations based on Mulliken electronegativities permit calculating flat band potentials in excellent agreement with measured ones and help with a preselection of pertinent electrode materials. The CB and VB positions for $BiVO_3F$ were calculated by $E_{VB/CB} = \chi - E^e \pm E_g/2$, χ being the geometric mean value of Mulliken electronegativity of the different atoms, E^e the free electron energy (E^e = 4.5 V vs SHE), and E_g the measured bandgap of the photocatalyst (∼1.8 eV); E_{VB} = 2.75 V and E_{CB} = 0.98 V vs SHE. This is reported in Figure 5c and compared to those calculated for $BiVO_4$. It shows potentialities for oxygen evolution as an anodic photocatalyst, similar to $BiVO_4$, as VB lies lower than the O_2/H_2O redox potential. In the actual scope, only the potentiality for photocurrent generation was investigated.

Photoactivated Transport. $BiVO_3F$ shows a positive slope in the Mott−Schottky plot $1/C^2(E)$ shown in Figure 6a, as expected for an n-type semiconductor, resulting in a flat band potential E_{fb} = 0.095 V vs Ag/AgCl or 0.684 vs RHE (pH = 6.5) at $1/C^2$ = 0.[41] This potential allows locating the valence and conduction band edges by knowing E_g and assuming that E_{fb} is lower by 0.1 V from the conduction band for n-type semiconductors.[42,43] Therefore, the conduction band potential

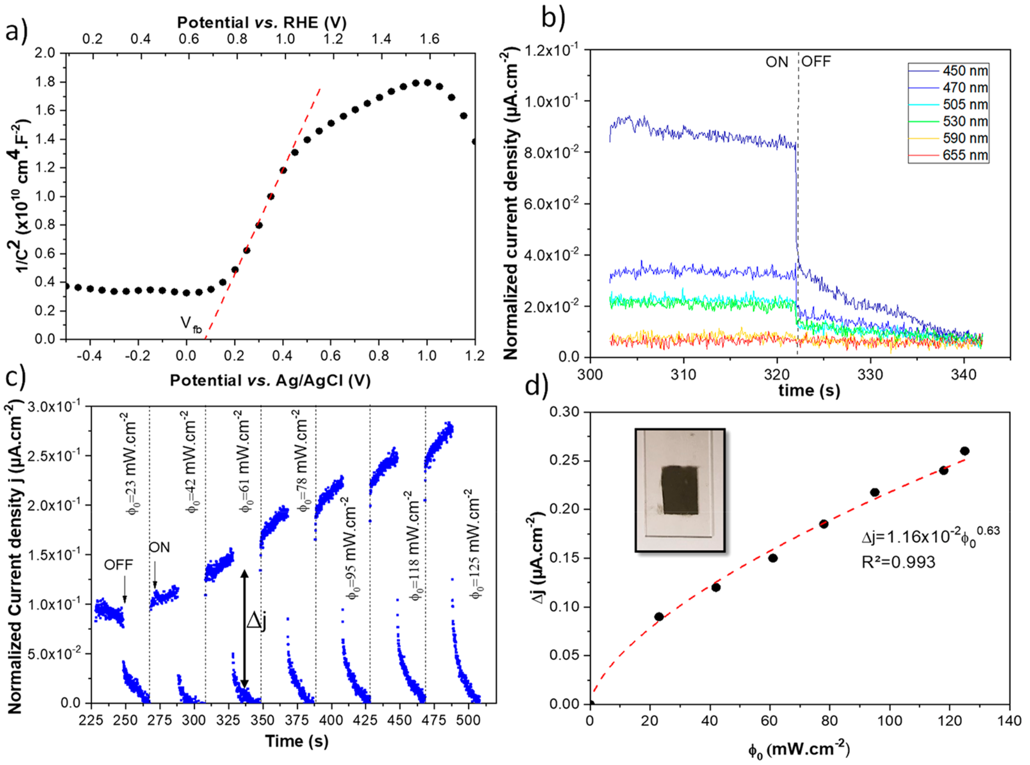

Figure 6. (a) Mott−Schottky plot for a $BiVO_3F$ film deposited on ITO/glass collected at 100 Hz (a 0.1 M sodium sulfate solution was used as the electrolyte). (b) Chronoamperometry (j−t) in the dark and under illumination for different wavelengths with a constant light beam intensity of 23 mW cm^{-2}. (c) Variation of normalized current density under illumination or in the dark depending on the intensity of the luminous flux (450 nm) and with an applied potential of 0.8 V vs Ag/AgCl. (d) Δj vs ϕ_0 plot and model in dotted lines (inset photograph of the film deposited by the drop-casting method).

of $BiVO_3F$ is consistent with the empirical calculated value given previously. Interestingly, in basic photoelectrochemical (PEC) water splitting, the photoinduced minority carriers are driven to the semiconductor/electrolyte interface, whereas the majority carriers are transported to the counter electrode through the external circuit.[44] In the case of an n-type semiconductor, electrons as the majority carriers are transferred to the counter electrode, while holes (the minority carriers) oxidize water to O_2 at the semiconductor surface. Therefore, n-type $BiVO_3F$ possesses both the carrier type and VB position for oxygen evolution, similarly to n-type $BiVO_4$.

The photoelectrochemical performances of this photoanode were studied in a three-electrode cell (Ag/ACl as the reference electrode and Pt as the counter electrode), and a 0.1 M Na_2SO_4 solution was used as electrolyte. The chronoamperometry results performed on a $BiVO_3F$ thick film are shown in Figure 6b and prove the generation of a modest photocurrent ($<10^{-1}$ μA/cm^2). The variation of the photocurrent density (Δj) shows better efficiency on increasing the irradiation energy, i.e., toward low wavelengths. A significant jump of the response is observed below 590 nm (above $\sim E_g$), which corresponds to the allowed $^2B_2 \rightarrow {}^2E$ transitions previously labeled as (1). At this stage, the strong magnetic exchange and poor Bi 6p participation favor an easy electron−hole recombination. In contrast, the current density increases drastically below 470 nm (2.6 eV), which corresponds to the allowed $^2B_2 \rightarrow {}^2B_1$, $^2A_1$ transitions (2) in the broad upper CB top part, for which the hybridization with Bi states would improve the electron−hole spatial separation and carrier extraction processes. The photocurrent response models rather well the specific CB topology, giving forbidden transitions between 2.2 and 2.5 eV; see Figure 5a.

The on/off variation at 450 nm is maximal for a photocurrent density of 0.09 μA cm^{-2} with a bias potential of 0.8 V vs Ag/AgCl and under a light intensity (ϕ_0) of 23 mW cm^{-2} (this drops to 0.02 μA cm^{-2} for 530 nm with the same luminous power and becomes equal to zero for higher wavelengths); see Figure 6c. The evolution of the photocurrent Δj with the intensity of the luminous flux (λ = 450 nm; V = 0.8 V vs Ag/AgCl) is shown in Figure 6d. It was fitted by a power law ($\Delta j = 1.6 \times 10^{-2}\ \phi_0{}^{0.63}$). The generation rate of photoelectrons by incident light (G_{pe}) is given by the expression[45,46]

$$G_{pe} = B_c n_{pe}(n_{pe} + M) \propto \phi_0 \tag{2}$$

where B_c is the recombination coefficient, n_{pe} is the density of photoelectrons, and M is number of impurity levels per cm^3. For $BiVO_3F$ $n_{pe} \gg$ M and eq 2 follows a power law:

$$\Delta j \propto n_{pe} = \sqrt{G_{pe}/B_c} \propto \phi_0{}^{1/2} \tag{3}$$

This suggests the dominant photocarrier decay mechanism is from e−h recombination rather than a trap-dominated recombination process. Despite the sharp, localized CB and VB as traps, spin-polarized dimers and a narrowed bandgap all in favor of longer carrier lifetimes, the dimerized crystal structure and the strong AFM exchanges make significant photoactivity difficult in our single-valent V^{4+} semiconductor, but inform as potentialities and novel concepts for $BiVO_3F$-type defects in a $BiVO_4$ structure. The similitude of the paired spins in $BiVO_3F$ with the monoclinic VO_2 behavior is also

https://doi.org/10.1021/jacs.1c00621
J. Am. Chem. Soc. 2021, 143, 6942−6951

reminiscent of some exotic features probably detrimental to any efficient charge−hole separation. In photoexcited monoclinic VO_2 a fast collapsing of the bandgap into a metal was observed by time-resolved photoelectron spectroscopy, at the femtosecond scale.[13] This ultrafast band structure reconstruction corresponds to the typical time announced for electron−hole formation and trapping in semiconducting TiO_2, suggesting a similar phenomenon in $BiVO_3F$ in spite of its larger bandgap, a major drawback for the further trapping of excitons, if available.

Note that for higher light intensities saturation can be achieved. Moreover, the photocurrent transient response follows an exponential-type evolution whose time constant increases with the light intensity. Finally, the response under solar excitation of AM1.5G 1-sun was also measured, showing the appearance of a photocurrent (Figure S2), scaled by the applied bias potential. A change from a crenel- to an exponential-type occurs upon increasing the applied potential.

■ CONCLUDING REMARKS

The discovery of novel stoichiometric mixed X = (O, F) compounds in the intensively studied Bi−V−X system is quite unexpected, enlarging the prism of the various specificities of the parent oxides, e.g., unequaled anionic conductivity in $Bi_2VO_{5.5}$ BIMEVOX Aurivillius derivatives[47] and Bi^{3+} square-planar coordination and field-dependent metal−insulator transition in $Bi_xV_8O_{16}$ hollandites.[48,49] $BiVO_3F$ is an original vanadyl $(V{=}O)^{2+}$ containing Bi-oxofluoride with alternating F_2 and O_2 μ_2 bridges along magnetically isolated chains. Despite short V═O bonds external to the chain axis, the crystal structure displays $V^{4+}-V^{4+}$ dimers (d = 2.93 Å) leading to $S = 0$ singlet dimers, $J/K_b \approx 300$ K, lacking long-range ordering. Several very promising results have been reported dealing with the photocatalytic properties of layered oxyhalides.[50−52] Here, the compositional analogy with $BiVO_4$ and electronic structure raises questions about the photoactivity of $BiVO_3F$. Despite its modest photoelectronic properties, $BiVO_3F$ provides clues for optimizing the photoanodic response by chemical design: (i) according to the chemical composition, filled Bi 6s orbitals hybridized with O 2p raise the VB edge and reduce the bandgap energy in $BiVO_4$ to $E_g = 2.4$ eV;[53] this is exaggerated in $BiVO_3F$ ($E_g = 1.7$ eV) by the incorporation of d^1 V^{4+} species. (ii) Theoretically, the visible light capture and conversion to photocurrent could reach ∼30% at this bandgap.[18] (iii) Sharp, localized d states at the top of the CB and bottom of the VB show analogies with defect carrier traps in d^n doped semiconductors. Additionally, several structural (Bi and V strongly asymmetric coordination, sp^2 oxygen atoms) and electronic band arguments are retained and validate the measured photoelectrical activity. However, the crystal structure itself with strongly coupled magnetic $V^{4+}-V^{4+}$ dimers is detrimental for d−d transitions and long electron−hole spatial separation. Further investigation of the electronic characteristic of $BiVO_3F$ is necessary at least in order to draw the $BiVO_3F/BiVO_4$ analogies and contrasts for a clear understanding of photocarrier specificities. It was observed that as soon as the energy reaches the upper CB zone with Bi hybridization, the photoconversion is greatly improved, which suggests that synthetic routes to antagonist 3D V^{4+} doped by halogen incorporation opens a promising route for specific components of high-performance photoelectric cells. Moreover, contrarily to most of the actual photocatalysts, $BiVO_3F$ film shows no sign of chemical- or photodegradation and thus offers clues to design more durable PEC technology. We recall that we did not observe any sign of chemical degradation nor photodegradation after our photocurrent study.

■ EXPERIMENTAL SECTION

Hydrothermal Synthesis. Single crystals were prepared through the hydrothermal route. A mixture of VF_3 (1 mmol) and Bi_2O_3 (1 mmol) was added together with 2.5 mL of deionized water and 0.5 mL of HF solution (7.65%) in a 23 mL Teflon-lined steel autoclave. The mixture was heated at 230 °C for 72 h and then cooled to room temperature. Products were successively washed with deionized water and ethanol and left to dry in air at room temperature. Black crystals were isolated for characterizations.

XRD. Powder XRD was carried out on a Bruker D8 Advanced diffractometer working in Bragg−Brentano geometry and using Cu radiation. The single crystal data collected on a Bruker X8 diffractometer (Ag Kα radiation) were treated using the Jana 2006 suite.[54] The powder data have been analyzed using the FULLPROF suite.[55]

Magnetic Measurement. Magnetic data and heat capacities were measured on a physical property measurement system, a Quantum Design PPMS DynaCool system, using $BiVO_3F$ ground powder.

UV−Visible Spectroscopy. It was measured on a PerkinElmer Lambda 650 spectrometer. The bandgap was calculated from the calculation of the Kubelka−Munk $F(R) = (1 - R^2)2R$ function and using a Tauc plot $(F(R) \times R \times E^{1/2})$ versus E, assuming direct allowed transitions.

DFT and EHTB Calculations. We performed density functional theory (DFT) band structure calculations using the full-potential local-orbital scheme (FPLO9.00-33)[56] applying the local density approximation (LDA+U, U = 2 to 4 eV) with the exchange−correlation potential by Perdew and Wang[57] using the Vienna *ab initio* simulation package (VASP)[58] with the basis set of projected augmented waves.[59] For the calculations of the magnetic exchanges identified in the text, we mapped the total energies for a number of collinear spin configurations onto a classical Heisenberg model to yield individual exchange couplings for various U and the effective on-site exchange interaction $J_{\mathrm{eff}} = 1$ eV. For the accurate DOS topology, the typical k mesh was 15 × 15 × 15 reduced to 1688 k-points in the symmetry-irreducible part of the first Brillouin zone for the crystallographic unit cell using the spin-polarized ferromagnetic configuration. The EHTB calculations have been performed using Samoa.[60]

Electrochemistry. Photoelectrochemical properties of $BiVO_3F$ were measured using a PGSTAT204 potentiostat/galvanostat (Metrohm) equipped with an electrochemical impedance spectroscopy (EIS) module and coupled with an optical bench consisting of low spectral dispersion LEDs or a 150 W Xe lamp (Quantum Design) with an AM1.5G filter (to simulate the terrestrial solar spectrum). For LED illumination sources, the intensity of the light beam as well as the excitation wavelength could be controlled by NOVA 2.0 software. The photoelectrochemical performance measurements were performed in a standard three-electrode cell (a Magnetic Mount photoelectrochemical cell (Redox.me) is used in order to obtain a standardized illumination of 1 cm^2 on the back face of the working electrode), and the electrolyte employed is an aqueous 0.1 M Na_2SO_4 solution. The working electrode consists of a thick $BiVO_3F$ film deposited on an ITO/glass substrate (Delta Technologies, Ltd.) by the drop-casting method. The crushed $BiVO_3F$ powder is added to a mixture of water and *N,N*-dimethylformamide (DMF) solvents with a 1:1 ratio. The liquid containing the suspension is drop-casted on the surface of the electrode, and a uniform layer is obtained after the solvent evaporation. A Ag/AgCl electrode and Pt wire were used as a reference and a counter electrode, respectively. The measured potentials versus the Ag/AgCl electrode were converted to the reversible hydrogen electrode (RHE) scale.

https://doi.org/10.1021/jacs.1c00621
J. Am. Chem. Soc. 2021, 143, 6942−6951

■ ASSOCIATED CONTENT

Supporting Information

The Supporting Information is available free of charge at https://pubs.acs.org/doi/10.1021/jacs.1c00621.

> More detailed crystallographic information (with powder refinement data, atomic positions, and anisotropic thermal displacement), with extra details on the synthesis and photoelectrochemical tests (PDF)

Accession Codes

CCDC 2055766 contains the supplementary crystallographic data for this paper. These data can be obtained free of charge via www.ccdc.cam.ac.uk/data_request/cif, or by emailing data_request@ccdc.cam.ac.uk, or by contacting The Cambridge Crystallographic Data Centre, 12 Union Road, Cambridge CB2 1EZ, UK; fax: +44 1223 336033.

■ AUTHOR INFORMATION

Corresponding Author

Olivier Mentré − *Université Lille, CNRS, Centrale Lille, Université Artois, UMR 8181, UCCS, Unité de Catalyse et Chimie du Solide, F-59000 Lille, France;* orcid.org/0000-0002-1822-6003; Email: Olivier.mentre@univ-lille.fr

Authors

Miguel A. Juárez-Rosete − *Université Lille, CNRS, Centrale Lille, Université Artois, UMR 8181, UCCS, Unité de Catalyse et Chimie du Solide, F-59000 Lille, France*

Sebastien Saitzek − *Université Lille, CNRS, Centrale Lille, Université Artois, UMR 8181, UCCS, Unité de Catalyse et Chimie du Solide, F-59000 Lille, France;* orcid.org/0000-0003-1403-5397

Cintli Aguilar-Maldonado − *Université Lille, CNRS, Centrale Lille, Université Artois, UMR 8181, UCCS, Unité de Catalyse et Chimie du Solide, F-59000 Lille, France*

Marie Colmont − *Université Lille, CNRS, Centrale Lille, Université Artois, UMR 8181, UCCS, Unité de Catalyse et Chimie du Solide, F-59000 Lille, France;* orcid.org/0000-0002-6120-0618

Ángel M. Arévalo-López − *Université Lille, CNRS, Centrale Lille, Université Artois, UMR 8181, UCCS, Unité de Catalyse et Chimie du Solide, F-59000 Lille, France;* orcid.org/0000-0002-8745-4990

Complete contact information is available at: https://pubs.acs.org/10.1021/jacs.1c00621

Notes

The authors declare no competing financial interest.

■ ACKNOWLEDGMENTS

This work was carried out under the framework of the LOVE-ME project supported by the ANR (Grant ANR ANR-16-CE08-0023). The Fonds Européen de Développement Régional (FEDER), CNRS, Région Hauts-de-France, and Ministère de l'Education Nationale, de l'Enseignement Supérieur et de la Recherche are acknowledged for funding the XRD and PPMS equipment. Chevreul Institute (FR 2638), Ministère de l'Education Nationale, de l'Enseignement Supérieur et de la Recherche, Région Hauts-de-France, FEDER, are acknowledged for supporting this work. The DIM 1 "Energetic efficiency" of the UArtois is thanked for its financial support for photoelectrochemical measurements. We thank Laurence Burylo, Nora Djelal, and Claire Minaud at the UCCS for their technical help. Hiroshi Kageyama and the JSPS Core-to-Core Program (A) Advanced Research Networks (JPJSCCA20200004) are acknowledged for motivating this "anion mixed material research" study.

■ REFERENCES

(1) Deng, D. Transition Metal Oxyfluorides for Next-Generation Rechargeable Batteries. *ChemNanoMat* **2017**, *3* (3), 146−159.

(2) Inaguma, Y.; Greneche, J. M.; Crosnier-Lopez, M. P.; Katsumata, T.; Calage, Y.; Fourquet, J. L. Structure and Mössbauer Studies of F-O Ordering in Antiferromagnetic Perovskite PbFeO2F. *Chem. Mater.* **2005**, *17* (6), 1386−1390.

(3) Simon, A.; Ravez, J. The Oxyfluoride Ferroelectrics. *Ferroelectrics* **1980**, *24* (1), 305−307.

(4) Katsumata, T.; Nakashima, M.; Umemoto, H.; Inaguma, Y. Synthesis of the Novel Perovskite-Type Oxyfluoride PbScO2F under High Pressure and High Temperature. *J. Solid State Chem.* **2008**, *181* (10), 2737−2740.

(5) Lemoine, K.; Lhoste, J.; Hémon-Ribaud, A.; Heidary, N.; Maisonneuve, V.; Guiet, A.; Kornienko, N. Investigation of Mixed-Metal (Oxy)Fluorides as a New Class of Water Oxidation Electrocatalysts. *Chem. Sci.* **2019**, *10* (40), 9209−9218.

(6) Mitoudi Vagourdi, E.; Müllner, S.; Lemmens, P.; Kremer, R. K.; Johnsson, M. Synthesis and Characterization of the Aurivillius Phase CoBi2O2F4. *Inorg. Chem.* **2018**, *57* (15), 9115−9121.

(7) Katsumata, T.; Suzuki, R.; Satoh, N.; Suzuki, S.; Nakashima, M.; Inaguma, Y.; Mori, D.; Aimi, A.; Yoneda, Y. Synthesis of New Perovskite-Type Oxyfluorides, BaInO2F and Comparison of the Structure among Perovskite-Type Oxyfluorides. *J. Solid State Chem.* **2019**, *279* (July), 120919.

(8) Leblanc, M.; Maisonneuve, V.; Tressaud, A. Crystal Chemistry and Selected Physical Properties of Inorganic Fluorides and Oxide-Fluorides. *Chem. Rev.* **2015**, *115* (2), 1191−1254.

(9) Tressaud, A.; Dance, J.-M. Relationships between Structure and Low-Dimensional Magnetism in Fluorides. *Structures versus Special Properties* **1982**, *52*, 87−146.

(10) Anke, B.; Rohloff, M.; Willinger, M. G.; Hetaba, W.; Fischer, A.; Lerch, M. Improved Photoelectrochemical Performance of Bismuth Vanadate by Partial O/F-Substitution. *Solid State Sci.* **2017**, *63*, 1−8.

(11) Akopjan, A. V.; Serov, T. V.; Dolgikh, V. A.; Ardaschnikova, E. I.; Lightfoot, P. A New Anion Conductive Bismuth-Vanadium Oxyfluoride. *J. Mater. Chem.* **2002**, *12* (5), 1490−1494.

(12) Wang, Z.; Huang, X.; Wang, X. Recent Progresses in the Design of BiVO4-Based Photocatalysts for Efficient Solar Water Splitting. *Catal. Today* **2019**, *335*, 31−38.

(13) Wegkamp, D.; Herzog, M.; Xian, L.; Gatti, M.; Cudazzo, P.; McGahan, C. L.; Marvel, R. E.; Haglund, R. F.; Rubio, A.; Wolf, M.; Stähler, J. Instantaneous Band Gap Collapse in Photoexcited Monoclinic VO2 Due to Photocarrier Doping. *Phys. Rev. Lett.* **2014**, *113* (21), DOI: 10.1103/PhysRevLett.113.216401.

(14) Zhao, Z.; Luo, W.; Li, Z.; Zou, Z. Density Functional Theory Study of Doping Effects in Monoclinic Clinobisvanite BiVO4. *Phys. Lett. A* **2010**, *374* (48), 4919−4927.

(15) Khan, H.; Swati, I. K. Fe3+-Doped Anatase TiO2 with d-d Transition, Oxygen Vacancies and Ti3+ Centers: Synthesis, Characterization, UV-Vis Photocatalytic and Mechanistic Studies. *Ind. Eng. Chem. Res.* **2016**, *55* (23), 6619−6633.

(16) Zhang, Y.; Guo, Y.; Duan, H.; Li, H.; Sun, C.; Liu, H. Facile Synthesis of V4+ Self-Doped, [010] Oriented BiVO4 Nanorods with Highly Efficient Visible Light-Induced Photocatalytic Activity. *Phys. Chem. Chem. Phys.* **2014**, *16* (44), 24519−24526.

(17) Jiang, H.; Dai, H.; Deng, J.; Liu, Y.; Zhang, L.; Ji, K. Porous F-Doped BiVO4: Synthesis and Enhanced Photocatalytic Performance for the Degradation of Phenol under Visible-Light Illumination. *Solid State Sci.* **2013**, *17*, 21−27.

(18) Jian, J.; Jiang, G.; van de Krol, R.; Wei, B.; Wang, H. Recent Advances in Rational Engineering of Multinary Semiconductors for

Photoelectrochemical Hydrogen Generation. *Nano Energy* **2018**, *51*, 457−480.

(19) Ellis, B. L.; Makahnouk, W. R.; Rowan-Weetaluktuk, W. N.; Ryan, D. H.; Nazar, L. F. Crystal Structure and Electrochemical Properties of A2MPO 4F Fluorophosphates (A = Na, Li; M = Fe, Mn, Co, Ni). *Chem. Mater.* **2010**, *22* (3), 1059−1070.

(20) Hu, S.; Johnsson, M.; Law, J. M.; Bettis, J. L.; Whangbo, M. H.; Kremer, R. K. Crystal Structure and Magnetic Properties of FeSeO3F - Alternating Antiferromagnetic S = 5/2 Chains. *Inorg. Chem.* **2014**, *53* (8), 4250−4256.

(21) Hu, S.; Johnsson, M. Synthesis and Crystal Structure of Two Synthetic Oxofluoride Framework Compounds - Co 2TeO 3F 2 and Co 2SeO 3F 2. *Dalt. Trans.* **2012**, *41* (41), 12786−12789.

(22) Mitoudi-Vagourdi, E.; Papawassiliou, W.; Müllner, S.; Jaworski, A.; Pell, A. J.; Lemmens, P.; Kremer, R. K.; Johnsson, M. Synthesis and Physical Properties of the Oxofluoride Cu2(SeO3)F2. *Inorg. Chem.* **2018**, *57* (8), 4640−4648.

(23) Streltsov, S. V.; Khomskii, D. I. Electronic Structure and Magnetic Properties of Pyroxenes (Li,Na) TM (Si,Ge)2 O6: Low-Dimensional Magnets with 90° Bonds. *Phys. Rev. B: Condens. Matter Mater. Phys.* **2008**, *77* (6), DOI: 10.1103/PhysRevB.77.064405.

(24) Gnezdilov, V.; Lemmens, P.; Zvyagin, A. A.; Cheranovskii, V. O.; Lamonova, K.; Pashkevich, Y. G.; Kremer, R. K.; Berger, H. Magnetic Crossover and Complex Excitation Spectrum of the Ferromagnetic/Antiferromagnetic Spin-1/2 Chain System α-TeVO4. *Phys. Rev. B: Condens. Matter Mater. Phys.* **2008**, *78* (18), DOI: 10.1103/PhysRevB.78.184407.

(25) Koo, H. J.; Whangbo, M. H. Spin Dimer Analysis of the Magnetic Structures of A2V3O9 (A = Ba, Sr) and η-Na9V14O35: Importance of the V4+-O···O-V4+ Super-Superexchange Interactions Mediated by the O-V5+-O Bridges. *Solid State Sci.* **2007**, *9* (9), 824−832.

(26) Aldous, D. W.; Lightfoot, P. Crystallisation of Some Mixed Na/V and K/V Fluorides by Solvothermal Methods. *Solid State Sci.* **2009**, *11* (2), 315−319.

(27) Pedersen, K. S.; Sigrist, M.; Weihe, H.; Bond, A. D.; Thuesen, C. A.; Simonsen, K. P.; Birk, T.; Mutka, H.; Barra, A. L.; Bendix, J. Magnetic Interactions through Fluoride: Magnetic and Spectroscopic Characterization of Discrete, Linearly Bridged [MnIII2(μ-F)F4-(Me3tacn)2](PF 6). *Inorg. Chem.* **2014**, *53* (10), 5013−5019.

(28) Goodenough, J. B.; Dutta, G.; Manthiram, A. Lattice Instabilities near the Critical V-V Separation for Localized versus Itinerant Electrons in LiV1-YMyO2 (M = Cr or Ti) Li1-XVO2. *Phys. Rev. B: Condens. Matter Mater. Phys.* **1991**, *43* (13), 10170−10178.

(29) Lakshmi, S.; Endo, T.; Siva, G. Electronic (Absorption) Spectra of 3d Transition Metal Complexes. *Advanced Aspects of Spectroscopy* **2012**, DOI: 10.5772/48089.

(30) Wang, C.; Wadhwa, A.; Cui, S.; Ma, R.; Qiao, X.; Fan, X.; Zhang, X. Dual Mode Temperature Sensing through Luminescence Lifetimes of F- and O-Coordinated Cr3+ Sites in Fluorosilicate Glass-Ceramics. *RSC Adv.* **2017**, *7* (83), 52435−52441.

(31) Kashimoto, Y.; Yonezawa, K.; Meissner, M.; Gruenewald, M.; Ueba, T.; Kera, S.; Forker, R.; Fritz, T.; Yoshida, H. The Evolution of Intermolecular Energy Bands of Occupied and Unoccupied Molecular States in Organic Thin Films. *J. Phys. Chem. C* **2018**, *122* (22), 12090−12097.

(32) Tsirlin, A. A.; Janson, O.; Rosner, H. Unusual Ferromagnetic Superexchange in CdVO3: The Role of Cd. *Phys. Rev. B: Condens. Matter Mater. Phys.* **2011**, *84* (14), DOI: 10.1103/PhysRevB.84.144429.

(33) Hall, J. W.; Marsh, W. E.; Weller, R. R.; Hatfield, W. E. Exchange Coupling in the Alternating-Chain Compounds Catena - Di-μ- Chlor o-Bis (4- Methy Lpy Ridine) Copper (II), ca Tena - Di-μ- Bromo- Bis (N- Methy Limidazole) Copper (II), Catena -[Hexanedione Bis(Thiosemicarbazonato)]Copper(II), and Catena -[Octaned. *Inorg. Chem.* **1981**, *20* (4), 1033−1037.

(34) Cooper, J. K.; Gul, S.; Toma, F. M.; Chen, L.; Glans, P. A.; Guo, J.; Ager, J. W.; Yano, J.; Sharp, I. D. Electronic Structure of Monoclinic BiVO4. *Chem. Mater.* **2014**, *26* (18), 5365−5373.

(35) Shao, Z.; Cao, X.; Luo, H.; Jin, P. Recent Progress in the Phase-Transition Mechanism and Modulation of Vanadium Dioxide Materials. *NPG Asia Mater.* **2018**, *10*, 581−605.

(36) Jacinto, M. J.; Ferreira, L. F.; Silva, V. C. Magnetic Materials for Photocatalytic Applications—a Review. *J. Sol-Gel Sci. Technol.* **2020**, *96*, 1.

(37) Gao, W.; Lu, J.; Zhang, S.; Zhang, X.; Wang, Z.; Qin, W.; Wang, J.; Zhou, W.; Liu, H.; Sang, Y. Suppressing Photoinduced Charge Recombination via the Lorentz Force in a Photocatalytic System. *Adv. Sci.* **2019**, *6* (18), 1901244.

(38) Pan, L.; Ai, M.; Huang, C.; Yin, L.; Liu, X.; Zhang, R.; Wang, S.; Jiang, Z.; Zhang, X.; Zou, J. J.; Mi, W. Manipulating Spin Polarization of Titanium Dioxide for Efficient Photocatalysis. *Nat. Commun.* **2020**, *11* (1), DOI: 10.1038/s41467-020-14333-w.

(39) Stahl, B.; Bredow, T. Critical Assessment of the DFT + U Approach for the Prediction of Vanadium Dioxide Properties. *J. Comput. Chem.* **2020**, *41* (3), 258−265.

(40) Butler, M. A.; Ginley, D. S. Prediction of Flatband Potentials at Semiconductor-Electrolyte Interfaces from Atomic Electronegativities. *J. Electrochem. Soc.* **1978**, *125* (2), 228−232.

(41) Bott, A. W. Electrocthemistry of Semiconductors. *Curr. Sep.* **1998**, *17* (3), 87−91.

(42) Kalanur, S. S. Structural, Optical, Band Edge and Enhanced Photoelectrochemical Water Splitting Properties of Tin-Doped WO3. *Catalysts* **2019**, *9* (5), 456.

(43) Matsumoto, Y.; Omae, M.; Watanabe, I.; Sato, E. Photoelectrochemical Properties of the Zn-Ti-Fe Spinel Oxides. *J. Electrochem. Soc.* **1986**, *133* (4), 711−716.

(44) Walter, M. G.; Warren, E. L.; McKone, J. R.; Boettcher, S. W.; Mi, Q.; Santori, E. A.; Lewis, N. S. Solar Water Splitting Cells. *Chem. Rev.* **2010**, *110* (11), 6446−6473.

(45) Moss, T. S. *Photoconductivity in the Elements*; Academic Press: New York, 1952.

(46) Ullrich, B.; Xi, H. Photocurrent Limit in Nanowires. *Opt. Lett.* **2013**, *38* (22), 4698.

(47) Lazure, S.; Vernochet, C.; Vannier, R. N.; Nowogrocki, G.; Mairesse, G. Composition Dependence of Oxide Anion Conduction in the BIMEVOX Family. *Solid State Ionics* **1996**, *90* (1−4), 117−123.

(48) Abraham, F.; Mentre, O. Bi1.7V8O16: The First Bi-Hollandite-Type Compound. *J. Solid State Chem.* **1994**, *109* (1), 127−133.

(49) Larson, A. M.; Wilfong, B.; Moetakef, P.; Brown, C. M.; Zavalij, P.; Rodriguez, E. E. Metal-Insulator Transition Tuned by Magnetic Field in Bi1.7V8O16 Hollandite. *J. Mater. Chem. C* **2017**, *5* (20), 4967−4976.

(50) Fujito, H.; Kunioku, H.; Kato, D.; Suzuki, H.; Higashi, M.; Kageyama, H.; Abe, R. Layered Perovskite Oxychloride Bi4NbO8Cl: A Stable Visible Light Responsive Photocatalyst for Water Splitting. *J. Am. Chem. Soc.* **2016**, *138* (7), 2082−2085.

(51) Kuriki, R.; Ichibha, T.; Hongo, K.; Lu, D.; Maezono, R.; Kageyama, H.; Ishitani, O.; Oka, K.; Maeda, K. A Stable, Narrow-Gap Oxyfluoride Photocatalyst for Visible-Light Hydrogen Evolution and Carbon Dioxide Reduction. *J. Am. Chem. Soc.* **2018**, *140* (21), 6648−6655.

(52) Nakada, A.; Kato, D.; Nelson, R.; Takahira, H.; Yabuuchi, M.; Higashi, M.; Suzuki, H.; Kirsanova, M.; Kakudou, N.; Tassel, C.; Yamamoto, T.; Brown, C. M.; Dronskowski, R.; Saeki, A.; Abakumov, A.; Kageyama, H.; Abe, R. Conduction Band Control of Oxyhalides with a Triple-Fluorite Layer for Visible Light Photocatalysis. *J. Am. Chem. Soc.* **2021**, *143* (6), 2491−2499.

(53) Walsh, A.; Yan, Y.; Huda, M. N.; Al-Jassim, M. M.; Wei, S. H. Band Edge Electronic Structure of BiVO 4: Elucidating the Role of the Bi s and V d Orbitals. *Chem. Mater.* **2009**, *21* (3), 547−551.

(54) Petrícek, V.; Dušek, M.; Palatinus, L. Crystallographic Computing System JANA2006: General Features. *Z. Kristallogr. - Cryst. Mater.* **2014**, *229*, 345−352.

(55) Rodríguez-Carvajal, J. Recent Advances in Magnetic Structure Determination by Neutron Powder Diffraction. *Phys. B* **1993**, *192* (1−2), 55−69.

(56) Koepernik, K.; Eschrig, H. Full-Potential Nonorthogonal Local-Orbital Minimum-Basis Band-Structure Scheme. *Phys. Rev. B - Condens. Matter Mater. Phys.* **1999**, *59* (3), 1743−1757.
(57) Perdew, J. P.; Wang, Y. Accurate and Simple Analytic Representation of the Electron-Gas Correlation Energy. *Phys. Rev. B: Condens. Matter Mater. Phys.* **1992**, *45* (23), 13244−13249.
(58) Kresse, G.; Hafner, J. Ab Initio Molecular Dynamics for Liquid Metals. *Phys. Rev. B: Condens. Matter Mater. Phys.* **1993**, *47* (1), 558.
(59) Blöchl, P. E. Projector Augmented-Wave Method. *Phys. Rev. B: Condens. Matter Mater. Phys.* **1994**, *50* (24), 17953−17979.
(60) Dai, D.; Ren, J.; Liang, W.; Whangbo, H. SAMOA (Structure and Molecular Orbital Analyzer); http://chvamw.chem.ncsu.edu/.